

1 **Title:** GABA-ergic dynamics in human frontotemporal networks confirmed by pharmaco-
2 magnetoencephalography.

3 **Abbreviated:** GABA networks by pharmaco-MEG.

4 **Authors:** Natalie E. Adams¹, Laura E. Hughes^{1,2}, Holly N. Phillips¹, Alexander D. Shaw², Alexander G.
5 Murley¹, David Nesbitt¹, Thomas E. Cope, W. Richard Bevan-Jones, Luca Passamonti, James B.
6 Rowe^{1,2}

7 ¹ Department of Clinical Neurosciences, Cambridge Biomedical Campus, University of Cambridge,
8 Cambridge, CB2 0QQ, UK

9 ² MRC Cognition and Brain Sciences Unit, 15 Chaucer Road, Cambridge, CB2 7EF, UK

10 ³ Cambridge Centre for Ageing and Neuroscience (Cam-CAN), University of Cambridge, UK

11 **Corresponding Author:** James B. Rowe, james.rowe@mrc-cbu.cam.ac.uk

12 **Number of Pages:** 38

13 **Number of Figures:** 4

14 **Number of Tables:** 1

15 **Number of Words for Abstract:** 210

16 **Number of Words for Introduction:** 650

17 **Number of Words for Discussion:** 1489

18 **Conflict of Interest:** The authors declare no competing financial interests.

19 **Acknowledgements:** This work was funded by the Wellcome Trust (103838), the National Institute
20 for Health Research Cambridge Biomedical Research Centre and the Medical Research Council
21 (MC_U105597119; MC_U_00005/12; SUAG/004/91365), Cambridge Centre for Parkinson-plus and
22 the Holt Fellowship. We thank the PSP Association & FTD Support Group for raising awareness of
23 the study. We also thank the School of Psychology, Cardiff University, 70 Park Pl, Cardiff, CF10 3AS,
24 UK.

25 **Abstract**

26 To bridge the gap between preclinical cellular models of disease and *in vivo* imaging of human
27 cognitive network dynamics, there is a pressing need for informative biophysical models. Here we
28 assess dynamic causal models (DCM) of cortical network responses, as generative models of
29 magnetoencephalographic observations during an auditory oddball roving paradigm in healthy
30 adults. This paradigm induces robust perturbations that permeate frontotemporal networks,
31 including an evoked ‘mismatch negativity’ response and transiently induced oscillations. Here, we
32 probe GABAergic influences of the networks using double-blind placebo-controlled randomised-
33 crossover administration of the GABA re-uptake inhibitor, tiagabine (oral, 10mg) in healthy older
34 adults. We demonstrate the facility of conductance-based neural mass mean-field models,
35 incorporating local synaptic connectivity, to investigate laminar-specific and GABAergic mechanisms
36 of the auditory response. The neuronal model accurately recapitulated the observed
37 magnetoencephalographic data. Using parametric empirical Bayes for optimal model inversion
38 across both drug sessions, we identify the effect of tiagabine on GABAergic modulation of deep
39 pyramidal and interneuronal cell populations. We found a transition of the main GABAergic drug
40 effects from auditory cortex in standard trials to prefrontal cortex in deviant trials. The successful
41 integration of pharmaco- magnetoencephalography with dynamic causal models of frontotemporal
42 networks provides a potential platform on which to evaluate the effects of disease and
43 pharmacological interventions.

44 **Significance Statement**

45 Understanding human brain function and developing new treatments require good models of brain
46 function. We tested a detailed generative model of cortical microcircuits that accurately reproduced
47 human magnetoencephalography, to quantify network dynamics and connectivity in frontotemporal
48 cortex. This approach identified the effect of a test drug (GABA-reuptake inhibitor, tiagabine) on
49 neuronal function (GABA-ergic dynamics), opening the way for psychopharmacological studies in
50 health and disease with the mechanistic precision afforded by generative models of the brain.

51

52 **Introduction**

53 Biophysically informed models of cognition and cognitive disorders facilitate the effective translation
54 of the mechanisms and treatments of disease. Recent progress towards detailed generative models
55 that replicate neurophysiological correlates of cognition based on cellular and network dynamics,
56 such as 'Dynamic Causal Models' (DCM), make predictions that approximate observations by
57 functional magnetic resonance imaging or electro- and magneto-encephalography (MEG) (Moran et
58 al., 2013). To be most useful, these models should incorporate laminar, cellular and synaptic
59 functions (Bastos et al., 2012), and adhere to basic principles of cortical connectivity (Shipp, 2016),
60 while also being sufficiently tractable and accurate to study cognition.

61 The DCM framework developed to meet these criteria, with applications in health and neurological
62 disorders (Kiebel et al., 2008; Stephan et al., 2008; Boly et al., 2011; Marreiros et al., 2015). DCMs
63 draw on empirical priors for synaptic time constants and conductances, together with a mean-field
64 forward model. They are optimised to match the observed neurophysiological data. DCMs are
65 supported by extensive data for face-validity (Stephan et al., 2008, 2015) and construct-validity (Razi
66 et al., 2015), but they must also achieve predictive validity (Moran et al., 2014; Gilbert and Moran,
67 2016; Shaw et al., 2018).

68 We tested the ability of DCMs to identify the effect of a pharmacological intervention. The DCMs
69 were designed to model human frontotemporal cortical networks during an auditory oddball
70 paradigm, with characteristic MEG responses to standard and deviant tones (<300ms). The
71 differential response to these tones (the Mismatch Negativity, MMN) is abnormal in many
72 neurological diseases (Boly et al., 2011; Naatanen et al., 2011; Hughes et al., 2013), reflecting a
73 change in prediction errors in hierarchical frontotemporal networks (Garrido et al., 2009b; Phillips et
74 al., 2015).

75 To examine laminar- and synaptic-dynamics in response to auditory stimuli we developed a new
76 DCM with six cell populations, called "ext-DCM". In six connected regions (locations from Phillips et

77 al., 2015, 2016), we used a conductance-based mean-field cortical modelling scheme (cf. Moran et
78 al., 2013; Marreiros et al., 2015). For auditory mismatch responses, both thalamocortical and
79 cortico-cortical connections integrate feedforward sensory inputs and feedback expectations. The
80 network architecture controls the flow and integration of information, via cell- and
81 neurotransmitter-specific interactions. The ext-DCM introduces new cortico-thalamic burst-firing
82 cells ('tp' in Figure 1a) that enable the model to generate beta activity from deep-layers (Roopun et
83 al., 2008a, 2010; Bordas et al., 2015; Michalareas et al., 2016). The ext-DCM also separates the
84 inhibitory interneuronal populations for superficial and deep pyramidal cells (e.g. Jiang *et al.*, 2015).
85 These extensions improve the DCMs' functionality in terms of laminar dynamics. We tested the
86 model's ability to accurately generate evoked magnetoencephalographic responses (i.e. event
87 related fields, ERF), under placebo and drug conditions.

88 With the ext-DCM, we used the drug tiagabine to test how well the neurophysiological model could
89 identify changes in the causes of observed neuronal dynamics. Tiagabine is a gamma-amino-butyric
90 acid (GABA) re-uptake inhibitor. GABA is critical for the generation of physiological responses and
91 rhythms in local and global processing (Whittington et al., 2000). This pharmacological specificity
92 provides a more controlled acute test of DCMs than autoimmune (Symmonds et al., 2018) and
93 genetic channelopathies (Gilbert et al., 2016).

94 Using parametric empirical Bayes to optimise the model across participants and drug conditions we
95 examined how modelled GABAergic dynamics are altered by tiagabine. Based on the hypothesis that
96 prediction and prediction error depend on short-term GABAergic plasticity (Castro-Alamancos and
97 Connors, 1996; Garrido et al., 2009a; Mongillo et al., 2018; Spriggs et al., 2018), we predicted that
98 upper and lower hierarchical frontotemporal processing would be differentially affected by tiagabine
99 during standard and deviant tones.

100 In summary, the study's principal aims were i) to introduce and assess the ext-DCM for generating
101 the event-related fields observed by MEG, ii) to identify receptor-specific changes that govern these
102 dynamics, comparing tiagabine and placebo treatment conditions, and iii) to assess whether these

103 pharmacological effects are expressed dynamically across trial types and regions with laminar
104 specificity.

105

106 **Materials and Methods**

107 *Experimental Design:*

108 We undertook a randomised placebo-controlled double-blind crossover study of the effects of
109 tiagabine in 20 healthy adults (aged 67.5 ± 4.2 , ten male). Participants had no neurological or
110 psychiatric illness and were recruited from the MRC Cognition and Brain Sciences and Join Dementia
111 Research volunteer panels. The study was approved by the Cambridge Research Ethics Committee
112 and written informed consent was acquired, in keeping with the declaration of Helsinki.

113 Neurophysiological responses were measured in an auditory roving oddball paradigm (Garrido et al.,
114 2008). Binaural sinusoidal tones were presented in phase via ear-pieces for 75 ms (with 7.5ms ramp
115 up and down at start and end of the tone), at 500 ms intervals. The frequency of the tone increased
116 or decreased in steps of 50 Hz (range 400 – 800 Hz). The change of frequency occurred after
117 between 3 and 10 repetitions, with a truncated exponential distribution that approximated a stable
118 expectancy of change over time. Auditory thresholds were assessed in quiet at 500, 1,000, and 1,500
119 Hz. Tones were presented at 60dB above the average threshold for a standard population through
120 the earpieces in the MEG.

121 Each participant attended two MEG sessions with a minimum two weeks interval. They received
122 either 10 mg oral tiagabine or a placebo, in randomised order. Bloods were taken 105 minutes later,
123 immediately prior to MEG data acquisition, to coincide with peak plasma levels and CNS penetration
124 (Nutt et al., 2015).

125 *Data Acquisition and pre-processing:*

126 Magnetoencephalography (MEG) used a 306-channel Vectorview acquisition system (Elekta
127 Neuromag, Helsinki) in a light Elekta Neuromag magnetically-shielded room. This consists of a pair of
128 gradiometers and a magnetometer at each of 102 locations, sampled at 1000 Hz. Vertical and
129 horizontal EOGs tracked eye movements and 5 head-position indicator coils tracked head position. A
130 MEG-Compatible 70 channel EEG cap (EasyCap GmbH) using Ag/AgCl electrodes positioned

131 according to the 10-20 system was used concurrently. A 3D digitizer (Fastrak Polhemus Inc.,
132 Colchester, VA) was used to record >100 scalp data points, nasion and bilateral pre-auricular
133 fiducials. Subjects also underwent T1-weighted structural magnetic resonance imaging (MPRAGE
134 sequence, TE = 2.9 ms, TR = 2000 ms, 1.1mm isotropic voxels) using a 3T Siemens PRISMA scanner.

135 MEG data pre-processing included head position alignment and movement compensation using 6
136 headcoils, placed around the head on the EEG cap, and employed the temporal extension of Signal
137 Space Separation with MaxFilter v2.2 (Elekta Neuromag). The auto-detection of bad channels was
138 combined with manual input of any channels logged as bad during data acquisition. The Statistical
139 Parametric Mapping toolbox (SPM12) (The Wellcome Trust Centre for Neuroimaging, UCL, UK) was
140 used for further pre-processing and analysis, in conjunction with modified and custom MATLAB
141 scripts (MATLAB 2017a, Mathworks, Natick, MA). Data were Butterworth filtered between 1 and 180
142 Hz, epoched from -100 ms to 400 ms relative to the auditory stimuli and artefact rejected using EOG,
143 EEG and MEG channel thresholding. Spectral analyses were performed using a multi-taper method.
144 The deviant trial was taken as the 1st trial of a train, regardless of the frequency and the 6th trial of a
145 train was modelled as 'standard'.

146 Source reconstruction used a forward model estimated using the single shell cortical mesh from
147 each individual's T1-weighted MR structural scan. After co-registration using the fiducials and head
148 points, local fields (LFs) for 6 sources of interest were source-reconstructed using SPM "COH"
149 method, a combination of LORETA and minimum norm (Pascual-Marqui et al., 1994; Heers et al.,
150 2016). Sources of interest were (with MNI coordinates in standard space following inverse
151 normalisation): left auditory cortex (LAud; -42, -22, 7), left superior temporal gyrus (LSTG; -61 -32 8),
152 left inferior frontal gyrus (LIFG; -46 20 8), right auditory cortex (RAud; 46, -14, 8), right superior
153 temporal gyrus (RSTG; 59 -25 8) and right inferior frontal gyrus (RIFG; 46 20 8). To create images of
154 induced power, SPM-LORETA was used for source localization of a 5 mm³ regular grid at the MMN
155 (150 – 250 ms) time window (100ms in width, regularization=0.05).

156 Correlation coefficients for comparing the actual and predicted ERFs were calculated using the
157 `corrcoef` function (Pearson correlation) in MATLAB 2017a for each individual, condition and node.

158 Time-frequency analysis was performed in SPM12 using a multi-taper method with 100 ms windows
159 overlapped by 5 ms and a bandwidth of 3. Frequency bands were split into alpha (8 – 13 Hz), beta
160 (14 – 29 Hz), low gamma (30 – 48 Hz) and high gamma (52 – 80 Hz).

161 *Neuronal Modelling: an extended canonical microcircuit model*

162 We used conductance-based canonical mean field (CMM) models for evoked responses (Kiebel et al.,
163 2008) utilising canonical microcircuit models (SPM12, DCM10). This approach to
164 neurophysiologically informed modelling using DCM goes beyond descriptive biomarkers by
165 providing a mechanistic link to realistic microscopic processes. A common approach in DCM is to
166 invert the neuronal and spatial forward model as a single generative model, to solve the source
167 reconstruction and biophysical modelling problems jointly by fitting the DCM to sensor data.
168 However, we modelled source specific responses to suppress conditional dependencies between the
169 neuronal parameters and the parameters of a spatial forward model. This affords more efficient
170 estimators of neuronal parameters, providing the source reconstruction is sufficiently precise given
171 the spatial topography of the network of interest. This has the advantage of compatibility with
172 multiple studies of this task (Muthukumaraswamy et al., 2015; Gilbert and Moran, 2016; Shaw et al.,
173 2017, 2018), including MEG and electrocorticography studies; the chosen network was based on the
174 published bilateral A1, STG, IFG networks associated with the generation of the MMN response.
175 Since this spatial element of the inverse problem was constrained, it is computationally more
176 appropriate to source localise using SPM with prior expected sources. The subsequent DCM was
177 then run on these virtual electrodes.

178 Our DCM included a conductance-based neural-mass model at each of the six anatomical locations,
179 as shown in Figure 1. We compared the default 4-cell conductance canonical-microcircuit model
180 with the ext-DCM, comprising 6 cell modules: a superficial pyramidal module (sp), a deep cortico-

181 cortical pyramidal module (dp), a thalamic-projection pyramidal module (tp), a granular stellate
182 module (ss) and separate supragranular and infragranular interneuron populations (si & di).
183 Excitatory autapses existed for all excitatory cell modules and all modules were also governed by an
184 inhibitory self-gain function that provided tonic inhibition to each module. The ext-DCM was
185 compared to the standard 4-cell model that is standard in SPM and is described in detail in Kiebel et
186 al. (2008). In summary, the 4-cell DCM lacks thalamocortical connectivity and has a unitary inhibitory
187 population interacting with all pyramidal and stellate cell populations.

188 The intrinsic connectivities are shown in Fig. 1a: note the excitatory conductances based on AMPA
189 and NMDA and inhibitory GABA-A and GABA-B conductances. The model is an extension of the SPM
190 conductance-based CMM model (SPM12, 2013): inclusion of separate supra- and infra-granular
191 interneuron populations creates a more biophysically realistic model that allows a greater flexibility
192 of independence of deep and superficial activity than in previous work (Bhatt et al., 2016; Shaw et
193 al., 2018; Spriggs et al., 2018). Additionally, the new 'tp' population expressed a hyperpolarization-
194 activated cation current (H-current) and a non-inactivating potassium current (M-current) to provide
195 surrogate intrinsic dynamics involved in the characteristic intrinsic bursting behaviour of these cells.
196 These two currents were fixed together with the reversal potential and the slope on the sigmoid
197 convolution of in-activation for the H-current (details of which parameters had a permitted variance
198 is given in Table 1). This, coupled with the cell capacitances, differentiates the intrinsic activation of
199 the 'tp' population from the 'dp' population. The populations also differed in their extrinsic
200 connectivities, with 'dp' populations forming cortico-cortical connections and 'tp' populations
201 allowing for cortico-thalamocortical connections. The thalamus was modelled implicitly, by an 80 ms
202 delay in connectivity with permitted variance.

203 Extrinsic connectivity between the six nodes is shown in Fig. 1b, with the detailed extrinsic
204 population connections shown in Fig. 1c. In keeping with the established principle of differential
205 cortical laminar projections of feed-forwards vs feedback connectivity (Bastos et al., 2012), backward
206 connections are facilitated by the 'dp' cells terminating on 'sp' and 'si' cells, whilst forward

207 connections run from 'sp' cells to 'ss' cells. Cortico-thalamo-cortical connections originate from 'tp'
208 cells and terminate following a thalamic delay at layer 4 'ss' cells. The presence or absence of
209 connections between nodes was based on the fully connected models from Phillips et al., (2015) and
210 Shaw et al., (2019), which in turn were derived from Garrido et al., (2008). This was used for the
211 basis of an iterative process to find the most likely reduced model (described below).

212 A Gaussian kernel (peak 60 ms, half-width 8 ms) represented auditory input to layer 4 stellates in
213 bilateral auditory and inferior frontal cortex.

214 *Bayesian Modelling and Statistical Analysis:*

215 We used Bayesian model inversion (estimation) and Bayesian model comparison (selection) to
216 identify the best explanation for subject-specific data, in terms of neuronal and biophysical
217 parameters. Parametric Empirical Bayes (PEB) was used for group inferences and to examine drug
218 effects, as described in Zeidman et al., (2019). By inverting a 'full' DCM per subject at the first level,
219 PEB avoids the problem of different first level DCMs falling into different local optima, and allows
220 subsequent comparison between conditions. At the second level, the parameters of interest were
221 included in the PEB, namely the GABAA synaptic connections. This restricted set of second level
222 parameters was oriented to our GABA-ergic hypothesis, and to improve stability of neural system
223 identifiability.

224 The DCM was run for each subject. Data were filtered between 0–48 Hz and a Tukey window was
225 applied that did not attenuate signals 50 ms before or 350 ms after stimuli. Inversion of the full
226 model was run separately for the standard and deviant trials and the parameter distributions passed
227 to second level Parametric Empirical Bayesian with contrasts for both trial types and drug conditions.
228 All intrinsic and extrinsic AMPA, NMDA and GABA-A conductance scalings could vary independently
229 in a manner that assumed symmetry between the two hemispheres. The prior means and permitted
230 variances are summarised in Table 1.

231 Variational Bayesian statistics using the Laplace approximation determined the probable parameter
232 space given the neuronal model and the data (Friston et al., 2007). The full model parameter space
233 was reduced by iteratively searching for dependencies in this parameter space and systematically
234 removing parameters not contributing to the free energy of the system (Henson et al., 2011). The
235 optimised reduced model comprises all those parameters and connections found to contribute
236 significantly to the system temporal dynamics. The comparison of full and reduced models is
237 conceptually analogous to F-tests in classical statistics, but inferences are Bayesian. A second-level
238 PEB was run, optimizing GABAA-ergic synaptic parameters (representing inhibitory gain). This second
239 level PEB identifies parameter that are estimated to differ significantly between task conditions, or
240 differ between drug-sessions, or for which there is a drug-by-condition interaction. The parameter
241 distributions from this reduced model were used to create a Bayesian model average of parameters
242 that differ significantly across the contrasts of trial types and drug conditions. The implementation of
243 PEB for model optimisation and contrast estimation is summarised in Fig. 1e.

244 For other data types, Bayesian t-tests reported in the main text used JASP (JASP Team 2019, version
245 0.10.2). Frequentist statistical methods reported in the main text used MATLAB (2017a, Mathworks,
246 Natick, MA).

247 *Code Accessibility:* The custom neuronal model used to generate these results is available at
248 [address on acceptance] and works in conjunction with SPM12.

249

250 **Results**

251 *Event related fields and induced spectral power*

252 Event related responses to standard and deviant trials were in line with previous findings (Hughes
253 and Rowe, 2013; Phillips et al., 2015, 2016) (Fig. 2a, first and second rows) and show the expected
254 M100, the primary response after the onset of a tone (80-120 ms), a difference signal (MMN)
255 between the standard and deviant trials (150-250 ms) and an M300 visible in frontal nodes (250-380
256 ms). The M100 was significantly reduced by tiagabine on standard and deviant trials, in left temporal
257 nodes (A1, and STG $p < 0.05$, paired t-test), whereas the later response leading into the M300 was
258 significantly reduced only on deviant trials in L/R IFG ($p < 0.05$, Bonferroni corrected for 6 regions).

259 The difference waveform (i.e. the deviant – the standard) reveals a typical biphasic MMN between
260 150-250ms, observed in primary auditory cortex and STG (Fig. 2a, third row). Tiagabine significantly
261 reduced the second peak of the MMN ($p < 0.05$) with bilateral IFG nodes and RSTG showing
262 reductions in the first peak of the mismatch response on tiagabine ($p < 0.05$). As with the deviant
263 response, LIFG showed a significant reduction of the later MMN peak and the M300 on tiagabine
264 ($p < 0.05$).

265 The temporal profile of spectral power differences (see Methods for time-frequency analysis)
266 matched that of the ERFs, including spectral counterparts to M100, MMN, continuing through the
267 M300 window (Fig. 2b&c). During the M100, alpha-power (8-12 Hz) decreases on tiagabine were
268 localized to temporal cortex and beta (14-29 Hz) decreases more prominently to posterior temporal
269 cortex. During the MMN, increases in low and high gamma (30-48 Hz and 52-80 Hz respectively)
270 were observed broadly across right frontal cortex, including IFG. Low gamma also showed increases
271 in right temporal cortex.

272 Such changes in the observed spatiotemporal physiology on tiagabine will be dependent on changes
273 in local and global network connectivity. The extended conductance-based dynamic causal model
274 was therefore used to infer the causes of the observed physiological changes.

275 *The Dynamical Causal Model:*

276 The residuals (difference between the actual and generated ERFs) were greater (worse) for the 4-cell
277 DCM than for the ext-DCM (Bayesian paired sample t-test: $BF=8.5 \times 10^{28}$) as shown in Fig. 3a. Bayesian
278 model comparison of the 4-cell *versus* ext-DCM confirmed that the ext-DCM performed better (ie.
279 was a more likely generator of the observed MEG) than the 4-cell DCM ($BF = 40.6$, Figure 3b). Note
280 that the model-evidences are corrected for differences in model complexity. Further analyses use
281 the ext-DCM only.

282 Fig. 3c demonstrates the evoked-response generated by the conductance-based dynamic causal
283 model at each node, for both drug conditions, using the optimal ext-DCM model as determined by
284 Parametric Empirical Bayes (see methods). Fig. 3d shows the correlation between generated and
285 observed data, for both standards' and deviants' responses, for both drug conditions at each node.
286 Boxplots indicate the spread of single-subject correlations across the group (open circles are
287 outliers), and black closed circles indicate the correlation of the mean response across all subjects
288 for each condition and node. Note how the periods of difference between the placebo and drug
289 conditions (black lines in Fig. 3c) are accurately generated (cf. 'predicted') by the model, with a high
290 match to the observed data in Fig. 2a.

291 The modelled responses are explained in terms of the parameters of the optimised model. Using
292 parametric empirical Bayes, condition effects on model parameters (connection and synaptic
293 parameters) were compared across the standard and deviant conditions, as well as across the
294 placebo and tiagabine conditions. Figure 4 shows the effect of tiagabine on the intrinsic GABAergic
295 connectivity, assuming symmetry (three bilateral averaged nodes are shown). We confirmed that
296 tiagabine significantly increases tonic GABAergic inhibition (posterior probability given for each
297 parameter in Fig. 4a). This was seen primarily in the deep layer pyramidal and interneuron
298 populations in primary auditory cortex and STG (Fig. 4a). An interaction between drug and condition
299 was found for the deep interneurons of Auditory cortex (posterior $p \approx 1.0$).

300 Fig. 4b compares GABA-A conductance scaling on deep interneurons between placebo and tiagabine
301 conditions, plotted for each individual. There was very strong evidence for differences between the
302 two drug conditions in primary auditory areas for the standard condition (BF=782356), and in IFG
303 and STG for the deviant condition (BF=3.58x10⁷ & BF=166 respectively). This difference between
304 primary auditory cortex and association cortex in STG/IFG, is in keeping with the functional
305 differentiation of upper versus lower levels in a hierarchical neural network with backwards
306 prediction and forward prediction error. Conversely, there was evidence of no difference between
307 the two drug conditions for the standard condition in IFG (BF=0.274) and for the deviant condition in
308 Aud (BF=0.241).

309 The correlation between tonic and phasic inhibition was explored for each region and condition. In
310 the frontal cortex, a strong negative relationship was found between the tonic inhibition of deep
311 inhibitory cells and their phasic inhibition onto cortico-thalamic cells (Fig. 4c Bayesian correlation
312 pairs, BF=398.43).

313

314 Discussion

315 The principal insights from this study are that an extended conductance-based canonical mean-field
316 method of dynamic causal modelling (a) succeeds in identifying the modulation of GABAergic
317 dynamics by the GABA-reuptake inhibitor tiagabine, and (b) is tractable and an accurate generator of
318 event-related fields that match those observed by magnetoencephalography, improving on an
319 earlier 4-cell model. Moreover, the ext-DCM suggests the effect of drug to be both laminar-specific
320 and dynamically modulated in different regions according to task condition. This opens the way for
321 psychopharmacological studies in health and disease with the mechanistic precision afforded by
322 using ext-DCMs as generative models.

323 We demonstrate that the intrinsic connectivity within hierarchical brain networks changes between
324 conditions in the mismatch task. The approach is of generalised relevance to hierarchical network
325 models of cognition such as speech (Cope et al., 2018), semantic (Adams et al., 2019) and visual
326 perception (Muthukumaraswamy *et al.*, 2013). Moreover, the laminar and pharmacological
327 specificity provided by the ext-DCM has the potential to quantify neuropathology in dementia,
328 developmental and psychiatric disorders (Duyckaerts et al., 1986; Kinoshita et al., 1996; Ferrer,
329 1999; Ji et al., 2018; Shaw et al., 2018).

330 *Understanding the MMN in terms of short-term plasticity.*

331 Tiagabine modulated the GABA-ergic dynamics across the trial types, implicating both local tonic- and
332 phasic effects. Repetitive activation with the same stimulus attenuated the ERF (reduction in N1/N2
333 by 6th repetition, Fig. 2). The model indicated higher tonic inhibition in the deep layers. We interpret
334 this as local short-term plastic changes in deep-layer inhibition (Knott et al., 2002; Hensch, 2005;
335 Jääskeläinen et al., 2007), regulating salient information (Mongillo et al., 2018).

336 The model suggested that tiagabine-induced increases of extracellular GABA leads to greater tonic
337 inhibition, consistent with overspill of GABA onto extra-synaptic receptors (Semyanov et al., 2004).

338 The effect was modulated differently in primary and associative processing areas: for tonic inhibition

339 of deep interneurons the drug's efficacy was highest in prefrontal cortex for deviant trials and in
340 auditory cortex for standard trials. In other words, GABAergic effects are modulated differentially in
341 upper and lower areas of the hierarchy dependent on the coding context. We speculate that this
342 reflects differential emphasis on beliefs (& feedback predictions) *versus* feedforward sensory
343 prediction errors in prefrontal versus primary auditory cortex; and that lower tonic inhibition at the
344 presentation of a deviant tone relates to homeostatic competition between phasic and tonic
345 inhibition (Wu et al., 2013). Increased phasic activation of deep-layer projections is necessary for
346 feedback of top-down information on context, which in turn increases phasic (and decreased tonic)
347 activation of deep interneurons. Decreasing tonic inhibition likely increases the interneuron
348 population activation (Semyanov et al., 2004), leading to increased phasic inhibition onto deep
349 pyramidal cells. This relationship was confirmed (Fig. 4c) between tonic inhibition of deep IFG
350 interneurons and phasic inhibition of deep IFG thalamic-projection neurons. Figure 4b shows that
351 whereas a drop in deep interneuron tonic inhibition was observed on deviant trials (*vs* standard),
352 tiagabine abolished the effect. It is to be expected that increases in exogenous GABA would increase
353 tonic GABAergic currents.

354 *GABA-ergic modulation of evoked and induced responses.*

355 Tiagabine affects oscillatory dynamics, which may influence behaviour (Coenen et al., 1995;
356 Magazzini et al., 2016; Port et al., 2017; Wyss et al., 2017). It remains a challenge to relate systemic
357 drug effects with local frequency-spectral phenomena. It has been proposed that beta-band activity
358 is associated with infragranular cortical projection neurons with intrinsically bursting profiles (Groh
359 et al., 2010; Roopun et al., 2010; Kim et al., 2015). We found that Tiagabine reduced the induced
360 beta-band activity in temporal areas. The model suggests that tonic inhibition is increased on
361 intrinsically bursting thalamic projection neurons in STG, which could increase rebound bursting via
362 intrinsic M- and H-currents (Roopun *et al.*, 2008; Roopun *et al.*, 2008b).

363 Conversely, it has been shown that gamma-band activity is dependent on the GABA-A receptor
364 activation and the phasic interplay of interneuron-pyramidal cell networks, particularly in the

365 superficial layers (Buffalo et al., 2011; Whittington et al., 2011). In the mismatch temporal window
366 (Fig. 2b) peak gamma increased occurring at the start of the mismatch period. This is consistent with
367 thalamic input (Di and Barth, 1992, 1993; Sukov and Barth, 2001) governing the envelope of gamma
368 activity in the superficial layers (Metherate and Cruikshank, 1999).

369 Overall, the observed dynamics and the model posterior parameters are consistent with knowledge
370 of network activation within the context of beta- and gamma- rhythm generation in cortex.

371 *Generative models of drug effects on cognitive physiology.*

372 Tiagabine's effect was largely confined to deep layers. As we modelled evoked activity it is difficult to
373 speculate on how this influences gamma activity across the network, however a reduction in deep-
374 layer influence may increase local cortical processing associated with gamma-band activity in the
375 superficial layers. As GABA levels are typically lower in older *versus* younger adults, tiagabine may
376 act 'restoratively'. This is corroborated with lower frequency responses that are dependent on GABA
377 (Mathias et al., 2001). Finally, we speculate that the reduced M100 on tiagabine results from the
378 widespread increased tonic inhibition represented in the model (Fig. 4), reducing local population
379 activity.

380 *Study limitations.*

381 Our study was motivated by the need for mechanistic studies of human cortical function, underlying
382 cognition, disease and therapeutics. Despite support for our three principal hypotheses, and
383 background validation studies (Moran et al., 2014), evidence from one study may not generalise to
384 other tasks and populations. There are study-specific considerations that limit our inferences, in
385 relation to our participants, our model, and drug of choice. For example, our participants were
386 healthy, and therefore have normal age related variance in GABA (Gao et al., 2013; Eavri et al.,
387 2018). They were older than those studied by Nutt et al (2015), and age-effects could interact with
388 the effects of tiagabine (Nutt et al., 2015). Our study was not designed to examine the effect of age

389 or ageing, but to focus on the normal brain in mid- and later-life. Further work would be required to
390 examine the effects of ageing on the ext-DCM.

391 Our model provides a simplified substrate for the neurophysiological processes. It is more detailed
392 than previous canonical microcircuit convolution models (Moran et al., 2013), in an effort to improve
393 the modelling of specific dynamics from distinct cell populations, their differing connectivities,
394 synaptic time constants and voltage-gated conductances. The extended model can produce a
395 spectrum of fast and slow responses, with fast responses involved in local processing dominated by
396 superficial layers and slower responses associated with feedback of information dominated by deep
397 layers (Roopun et al., 2006; Kramer et al., 2008; Whittington et al., 2011). It can incorporate delayed
398 activity associated with local, cortico-cortical and cortico-thalamo-cortical connections. Currently,
399 this system is a simplified network acting as a neural mass, and can represent relevant cortical
400 interactions involved in ERF generation in the context of this task and study. It does this by allowing
401 forward and backward modulation of activity between deep and superficial layers, where synaptic
402 time constants corroborate with standard GABA, NMDA and AMPA receptor decays. The six
403 specified nodes are commonly cited in the literature in the context of this task (Garrido et al., 2009b;
404 Phillips et al., 2015). Although they are not a complete representation of possible network
405 configurations, they have been shown to capture critical aspects of cortical function: here the
406 network has been supplemented with modelled exogenous and endogenous inputs via thalamus.

407 We emphasise Bayesian statistical analyses over classical frequentist methods. Where parameter
408 estimates derived from earlier DCMs are used for frequentist statistical tests, they have excellent
409 reliability across sessions, and similar power to fMRI and EEG studies (Rowe et al., 2010; Goulden et
410 al., 2012; Bernal-Casas et al., 2013). Frequentist approaches are familiar to many readers, and have
411 been the norm for comparison of ERFs, and we therefore include them selectively. Such a
412 frequentist approach is surpassed by the direct inferences on posterior probability inherent in DCMs
413 Bayesian inference, including PEB.

414 Tiagabine is a relatively specific blocker of GAT-1 at the concentrations used, but does not
415 distinguish between the mechanisms activated by GABA (Bowery et al., 1987; Mody and Pearce,
416 2004; Lee and Maguire, 2014). The timing of the magnetoencephalography coincided with expected
417 peak plasma levels, but levels may vary between individuals and future studies could include levels
418 as a covariate of interest, or model time-varying responses in relation to drug levels
419 (Muthukumaraswamy et al., 2013b).

420 In conclusion, we have used a conductance-based model of cortical neuronal dynamics to study
421 GABA-ergic interactions and probe laminar-specific physiological responses to tiagabine. The model
422 accurately generated physiological data that matched the MEG responses and confirmed the effect
423 of tiagabine on tonic GABA-A inhibitory gain within frontal and temporal cortical circuits. Our data
424 provide support for mechanistic studies of neurological disorders, including but not limited to
425 GABAergic impairments (Murley and Rowe, 2018). They also point to new approaches for
426 experimental medicine studies in humans that aim for the laminar, cellular or synaptic precision
427 made possible in new generations of dynamic causal models.

428

429

430 **Acknowledgements**

431 This work was funded by the Wellcome Trust (103838), the National Institute for Health Research
432 Cambridge Biomedical Research Centre and the Medical Research Council (MC_U105597119 &
433 MC_U_00005/12), Cambridge Centre for Parkinson-plus and Holt Fellowship. We thank the PSP
434 Association & FTD Support Group for raising awareness of the study.

435

436

437 **References**

- 438 Adams NE, Teige C, Mollo G, Karapanagiotidis T, Cornelissen PL, Smallwood J, Traub RD, Jefferies E,
439 Whittington MA (2019) Theta/delta coupling across cortical laminae contributes to semantic
440 cognition. *J Neurophysiol*:jn.00686.2018 Available at:
441 <https://www.physiology.org/doi/10.1152/jn.00686.2018> [Accessed January 31, 2019].
- 442 Bastos AM, Usrey WM, Adams RA, Mangun GR, Fries P, Friston KJ (2012) Canonical Microcircuits for
443 Predictive Coding. *Neuron* 76:695–711 Available at:
444 <https://www.sciencedirect.com/science/article/pii/S0896627312009592> [Accessed January 15,
445 2019].
- 446 Bernal-Casas D, Balaguer-Ballester E, Gerchen MF, Iglesias S, Walter H, Heinz A, Meyer-Lindenberg A,
447 Stephan KE, Kirsch P (2013) Multi-site reproducibility of prefrontal–hippocampal connectivity
448 estimates by stochastic DCM. *Neuroimage* 82:555–563 Available at:
449 <https://www.sciencedirect.com/science/article/pii/S1053811913006307> [Accessed March 1,
450 2019].
- 451 Bhatt MB, Bowen S, Rossiter HE, Dupont-Hadwen J, Moran RJ, Friston KJ, Ward NS (2016)
452 Computational modelling of movement-related beta-oscillatory dynamics in human motor
453 cortex. *Neuroimage* 133:224–232 Available at:
454 <https://www.sciencedirect.com/science/article/pii/S1053811916001981#f0005> [Accessed
455 January 15, 2019].
- 456 Boly M, Garrido MI, Gosseries O, Bruno M-A, Boveroux P, Schnakers C, Massimini M, Litvak V,
457 Laureys S, Friston K (2011) Preserved Feedforward But Impaired Top-Down Processes in the
458 Vegetative State. *Science* (80-) 332:858–862 Available at:
459 <http://www.ncbi.nlm.nih.gov/pubmed/21566197> [Accessed February 26, 2019].
- 460 Bordas C, Kovacs A, Pal B (2015) The M-current contributes to high threshold membrane potential
461 oscillations in a cell type-specific way in the pedunculopontine nucleus of mice. *Front Cell*

462 Neurosci 9:121 Available at:
463 <http://journal.frontiersin.org/article/10.3389/fncel.2015.00121/abstract> [Accessed March 1,
464 2019].

465 Bowery NG, Hudson AL, Price GW (1987) GABAA and GABAB receptor site distribution in the rat
466 central nervous system. *Neuroscience* 20:365–383 Available at:
467 <https://www.sciencedirect.com/science/article/pii/0306452287900984> [Accessed September
468 11, 2018].

469 Buffalo EA, Fries P, Landman R, Buschman TJ, Desimone R (2011) Laminar differences in gamma and
470 alpha coherence in the ventral stream. *Proc Natl Acad Sci U S A* 108:11262–11267.

471 Castro-Alamancos MA, Connors BW (1996) Cellular mechanisms of the augmenting response: short-
472 term plasticity in a thalamocortical pathway. *J Neurosci* 16:7742–7756 Available at:
473 <http://www.ncbi.nlm.nih.gov/pubmed/8922430> [Accessed June 19, 2018].

474 Coenen AML, Blezer EHM, van Luijtelaar ELJM (1995) Effects of the GABA-uptake inhibitor tiagabine
475 on electroencephalogram, spike-wave discharges and behaviour of rats. *Epilepsy Res* 21:89–94
476 Available at: <https://www.sciencedirect.com/science/article/pii/0920121195000153> [Accessed
477 February 26, 2019].

478 Di S, Barth DS (1992) The functional anatomy of middle-latency auditory evoked potentials:
479 thalamocortical connections. *J Neurophysiol* 68:425–431 Available at:
480 <http://www.ncbi.nlm.nih.gov/pubmed/1382119> [Accessed September 5, 2018].

481 Di S, Barth DS (1993) Binaural vs. monaural auditory evoked potentials in rat neocortex. *Brain Res*
482 630:303–314 Available at:
483 <https://www.sciencedirect.com/science/article/pii/0006899393906701> [Accessed September 5,
484 2018].

485 Duyckaerts C, Hauw J-J, Bastenaire F, Piette F, Poulain C, Rainsard V, Javoy-Agid F, Berthaux P (1986)

486 Laminar distribution of neocortical senile plaques in senile dementia of the alzheimer type.
487 Acta Neuropathol 70:249–256 Available at: <http://link.springer.com/10.1007/BF00686079>
488 [Accessed January 15, 2019].

489 Eavri R, Shepherd J, Welsh CA, Flanders GH, Bear M, Nedivi E (2018) Interneuron simplification and
490 loss of structural plasticity as markers of aging-related functional decline. J Neurosci:0808–
491 0818 Available at: <http://www.ncbi.nlm.nih.gov/pubmed/30108129> [Accessed August 22,
492 2018].

493 Ferrer I (1999) Neurons and their dendrites in frontotemporal dementia. Dement Geriatr Cogn
494 Disord 10 Suppl 1:55–60 Available at: <http://www.ncbi.nlm.nih.gov/pubmed/10436342>
495 [Accessed August 22, 2018].

496 Friston K, Mattout J, Trujillo-Barreto N, Ashburner J, Penny W (2007) Variational free energy and the
497 Laplace approximation. Neuroimage 34:220–234 Available at:
498 <https://www.sciencedirect.com/science/article/pii/S1053811906008822> [Accessed May 1,
499 2018].

500 Gao F, Edden RAE, Li M, Puts NAJ, Wang G, Liu C, Zhao B, Wang H, Bai X, Zhao C, Wang X, Barker PB
501 (2013) Edited magnetic resonance spectroscopy detects an age-related decline in brain GABA
502 levels. Neuroimage 78:75–82 Available at:
503 <https://www.sciencedirect.com/science/article/pii/S105381191300339X> [Accessed September
504 4, 2018].

505 Garrido MI, Friston KJ, Kiebel SJ, Stephan KE, Baldeweg T, Kilner JM (2008) The functional anatomy of
506 the MMN: a DCM study of the roving paradigm. Neuroimage 42:936–944 Available at:
507 <https://linkinghub.elsevier.com/retrieve/pii/S1053811908006484> [Accessed January 8, 2019].

508 Garrido MI, Kilner JM, Kiebel SJ, Stephan KE, Baldeweg T, Friston KJ (2009a) Repetition suppression
509 and plasticity in the human brain. Neuroimage 48:269–279 Available at:
510 <https://www.sciencedirect.com/science/article/pii/S1053811909006661> [Accessed January 8,

511 2019].

512 Garrido MI, Kilner JM, Stephan KE, Friston KJ (2009b) The mismatch negativity: a review of
513 underlying mechanisms. *Clin Neurophysiol* 120:453–463 Available at:
514 <http://www.ncbi.nlm.nih.gov/pubmed/19181570> [Accessed May 1, 2018].

515 Gilbert JR, Moran RJ (2016) Inputs to prefrontal cortex support visual recognition in the aging brain.
516 *Sci Rep* 6:31943 Available at: <http://www.nature.com/articles/srep31943> [Accessed January
517 14, 2019].

518 Gilbert JR, Symmonds M, Hanna MG, Dolan RJ, Friston KJ, Moran RJ (2016) Profiling neuronal ion
519 channelopathies with non-invasive brain imaging and dynamic causal models: Case studies of
520 single gene mutations. *Neuroimage* 124:43–53 Available at:
521 <https://www.sciencedirect.com/science/article/pii/S1053811915007788> [Accessed July 8,
522 2019].

523 Goulden N, Elliott R, Suckling J, Williams SR, Deakin JFW, McKie S (2012) Sample Size Estimation for
524 Comparing Parameters Using Dynamic Causal Modeling. *Brain Connect* 2:80–90 Available at:
525 <http://www.liebertpub.com/doi/10.1089/brain.2011.0057> [Accessed March 1, 2019].

526 Groh A, Meyer HS, Schmidt EF, Heintz N, Sakmann B, Krieger P (2010) Cell-Type Specific Properties of
527 Pyramidal Neurons in Neocortex Underlying a Layout that Is Modifiable Depending on the
528 Cortical Area. *Cereb Cortex* 20:826–836 Available at:
529 <http://www.ncbi.nlm.nih.gov/pubmed/19643810> [Accessed June 19, 2018].

530 Heers M, Chowdhury RA, Hedrich T, Dubeau F, Hall JA, Lina J-M, Grova C, Kobayashi E (2016)
531 Localization Accuracy of Distributed Inverse Solutions for Electric and Magnetic Source Imaging
532 of Interictal Epileptic Discharges in Patients with Focal Epilepsy. *Brain Topogr* 29:162–181
533 Available at: <http://link.springer.com/10.1007/s10548-014-0423-1> [Accessed December 18,
534 2018].

535 Hensch TK (2005) Critical period plasticity in local cortical circuits. *Nat Rev Neurosci* 6:877–888
536 Available at: <http://www.nature.com/articles/nrn1787> [Accessed August 22, 2018].

537 Henson RN, Wakeman DG, Litvak V, Friston KJ (2011) A Parametric Empirical Bayesian Framework for
538 the EEG/MEG Inverse Problem: Generative Models for Multi-Subject and Multi-Modal
539 Integration. *Front Hum Neurosci* 5:76 Available at:
540 <http://journal.frontiersin.org/article/10.3389/fnhum.2011.00076/abstract> [Accessed May 1,
541 2018].

542 Hughes LE, Ghosh BCP, Rowe JB (2013) Reorganisation of brain networks in frontotemporal
543 dementia and progressive supranuclear palsy. *NeuroImage Clin* 2:459–468 Available at:
544 <https://www.sciencedirect.com/science/article/pii/S2213158213000302> [Accessed October 24,
545 2018].

546 Hughes LE, Rowe JB (2013) The Impact of Neurodegeneration on Network Connectivity: A Study of
547 Change Detection in Frontotemporal Dementia. *J Cogn Neurosci* 25:802–813 Available at:
548 http://www.mitpressjournals.org/doi/10.1162/jocn_a_00356 [Accessed January 15, 2019].

549 Jääskeläinen IP, Ahveninen J, Belliveau JW, Raij T, Sams M (2007) Short-term plasticity in auditory
550 cognition. *Trends Neurosci* 30:653–661 Available at:
551 <https://www.sciencedirect.com/science/article/pii/S0166223607002585> [Accessed June 26,
552 2018].

553 Ji E, Samuel S, Leboyer M, Guevara M, Guevara P, Poupon C, Grigis A, Houenou J (2018) T145.
554 ALTERATIONS IN SUPERFICIAL WHITE MATTER IN THE FRONTAL CORTEX IN SCHIZOPHRENIA: A
555 DWI STUDY USING A NOVEL ATLAS. *Schizophr Bull* 44:S172–S172 Available at:
556 https://academic.oup.com/schizophreniabulletin/article/44/suppl_1/S172/4957486 [Accessed
557 January 15, 2019].

558 Jiang X, Shen S, Cadwell CR, Berens P, Sinz F, Ecker AS, Patel S, Tolias AS (2015) Principles of
559 connectivity among morphologically defined cell types in adult neocortex. *Science* (80-)

560 350:aac9462–aac9462 Available at: <http://www.ncbi.nlm.nih.gov/pubmed/26612957>
561 [Accessed March 1, 2019].

562 Kiebel SJ, Garrido MI, Moran RJ, Friston KJ (2008) Dynamic causal modelling for EEG and MEG. *Cogn*
563 *Neurodyn* 2:121–136 Available at: <http://link.springer.com/10.1007/s11571-008-9038-0>
564 [Accessed January 14, 2019].

565 Kim EJ, Juavinett AL, Kyubwa EM, Jacobs MW, Callaway EM (2015) Three Types of Cortical Layer 5
566 Neurons That Differ in Brain-wide Connectivity and Function. *Neuron* 88:1253–1267 Available
567 at: <https://www.sciencedirect.com/science/article/pii/S0896627315009812> [Accessed
568 September 4, 2018].

569 Kinoshita A, Tomimoto H, Tachibana N, Suenaga T, Kawamata T, Kimura T, Akiguchi I, Kimura J (1996)
570 A case of primary progressive aphasia with abnormally ubiquitinated neurites in the cerebral
571 cortex. *Acta Neuropathol* 92:520–524 Available at:
572 <http://link.springer.com/10.1007/s004010050555> [Accessed January 15, 2019].

573 Knott GW, Quairiaux C, Genoud C, Welker E (2002) Formation of dendritic spines with GABAergic
574 synapses induced by whisker stimulation in adult mice. *Neuron* 34:265–273 Available at:
575 <http://www.ncbi.nlm.nih.gov/pubmed/11970868> [Accessed January 3, 2019].

576 Kramer MA, Roopun AK, Carracedo LM, Traub RD, Whittington MA, Kopell NJ (2008) Rhythm
577 Generation through Period Concatenation in Rat Somatosensory Cortex Friston KJ, ed. *PLoS*
578 *Comput Biol* 4:e1000169 Available at: <https://dx.plos.org/10.1371/journal.pcbi.1000169>
579 [Accessed February 26, 2019].

580 Lee V, Maguire J (2014) The impact of tonic GABAA receptor-mediated inhibition on neuronal
581 excitability varies across brain region and cell type. *Front Neural Circuits* 8:3 Available at:
582 <http://journal.frontiersin.org/article/10.3389/fncir.2014.00003/abstract> [Accessed June 27,
583 2018].

584 Magazzini L, Muthukumaraswamy SD, Campbell AE, Hamandi K, Lingford-Hughes A, Myers JFM, Nutt
585 DJ, Sumner P, Wilson SJ, Singh KD (2016) Significant reductions in human visual gamma
586 frequency by the gaba reuptake inhibitor tiagabine revealed by robust peak frequency
587 estimation. *Hum Brain Mapp* 37:3882–3896 Available at:
588 <http://www.ncbi.nlm.nih.gov/pubmed/27273695> [Accessed February 26, 2019].

589 Marreiros AC, Pinotsis DA, Brown P, Friston KJ (2015) DCM, Conductance Based Models and Clinical
590 Applications. In, pp 43–70. Springer, Cham. Available at: [http://link.springer.com/10.1007/978-](http://link.springer.com/10.1007/978-3-319-20037-8_3)
591 [3-319-20037-8_3](http://link.springer.com/10.1007/978-3-319-20037-8_3) [Accessed January 15, 2019].

592 Mathias S, Wetter TC, Steiger A, Lancel M (2001) The GABA uptake inhibitor tiagabine promotes slow
593 wave sleep in normal elderly subjects. *Neurobiol Aging* 22:247–253 Available at:
594 <http://www.ncbi.nlm.nih.gov/pubmed/11182474> [Accessed May 1, 2018].

595 Metherate R, Cruikshank SJ (1999) Thalamocortical inputs trigger a propagating envelope of gamma-
596 band activity in auditory cortex in vitro. *Exp Brain Res* 126:160–174 Available at:
597 <http://link.springer.com/10.1007/s002210050726> [Accessed June 19, 2018].

598 Michalareas G, Vezoli J, van Pelt S, Schoffelen J-M, Kennedy H, Fries P (2016) Alpha-Beta and Gamma
599 Rhythms Subserve Feedback and Feedforward Influences among Human Visual Cortical Areas.
600 *Neuron* 89:384–397 Available at: <http://www.ncbi.nlm.nih.gov/pubmed/26777277> [Accessed
601 March 1, 2019].

602 Mody I, Pearce RA (2004) Diversity of inhibitory neurotransmission through GABAA receptors.
603 *Trends Neurosci* 27:569–575 Available at:
604 <https://www.sciencedirect.com/science/article/pii/S0166223604002279> [Accessed September
605 11, 2018].

606 Mongillo G, Rumpel S, Loewenstein Y (2018) Inhibitory connectivity defines the realm of excitatory
607 plasticity. *Nat Neurosci* 21:1463–1470 Available at: [http://www.nature.com/articles/s41593-](http://www.nature.com/articles/s41593-018-0226-x)
608 [018-0226-x](http://www.nature.com/articles/s41593-018-0226-x) [Accessed December 5, 2018].

609 Moran R, Pinotsis DA, Friston K (2013) Neural masses and fields in dynamic causal modeling. *Front*
610 *Comput Neurosci* 7:57 Available at:
611 <http://journal.frontiersin.org/article/10.3389/fncom.2013.00057/abstract> [Accessed January 3,
612 2019].

613 Moran RJ, Symmonds M, Dolan RJ, Friston KJ (2014) The Brain Ages Optimally to Model Its
614 Environment: Evidence from Sensory Learning over the Adult Lifespan Sporns O, ed. *PLoS*
615 *Comput Biol* 10:e1003422 Available at: <https://dx.plos.org/10.1371/journal.pcbi.1003422>
616 [Accessed February 26, 2019].

617 Murley AG, Rowe JB (2018) Neurotransmitter deficits from frontotemporal lobar degeneration. *Brain*
618 141:1263–1285 Available at: <https://academic.oup.com/brain/article/141/5/1263/4823510>
619 [Accessed October 24, 2018].

620 Muthukumaraswamy SD, Myers JFM, Wilson SJ, Nutt DJ, Hamandi K, Lingford-Hughes A, Singh KD
621 (2013a) Elevating Endogenous GABA Levels with GAT-1 Blockade Modulates Evoked but Not
622 Induced Responses in Human Visual Cortex. *Neuropsychopharmacology* 38:1105–1112
623 Available at: <http://www.nature.com/articles/npp20139> [Accessed May 1, 2018].

624 Muthukumaraswamy SD, Myers JFM, Wilson SJ, Nutt DJ, Lingford-Hughes A, Singh KD, Hamandi K
625 (2013b) The effects of elevated endogenous GABA levels on movement-related network
626 oscillations. *Neuroimage* 66:36–41 Available at:
627 <https://www.sciencedirect.com/science/article/pii/S1053811912010579?via%3Dihub>
628 [Accessed February 26, 2019].

629 Muthukumaraswamy SD, Shaw AD, Jackson LE, Hall J, Moran R, Saxena N (2015) Evidence that
630 Subanesthetic Doses of Ketamine Cause Sustained Disruptions of NMDA and AMPA-Mediated
631 Frontoparietal Connectivity in Humans. *J Neurosci* 35:11694–11706 Available at:
632 <http://www.ncbi.nlm.nih.gov/pubmed/26290246> [Accessed January 14, 2019].

633 Naatanen R, Kujala T, Kreegipuu K, Carlson S, Escera C, Baldeweg T, Ponton C (2011) The mismatch

634 negativity: an index of cognitive decline in neuropsychiatric and neurological diseases and in
635 ageing. *Brain* 134:3435–3453 Available at: [https://academic.oup.com/brain/article-](https://academic.oup.com/brain/article-lookup/doi/10.1093/brain/awr064)
636 [lookup/doi/10.1093/brain/awr064](https://academic.oup.com/brain/article-lookup/doi/10.1093/brain/awr064) [Accessed February 26, 2019].

637 Nutt D, Wilson S, Lingford-Hughes A, Myers J, Papadopoulos A, Muthukumaraswamy S (2015)
638 Differences between magnetoencephalographic (MEG) spectral profiles of drugs acting on
639 GABA at synaptic and extrasynaptic sites: A study in healthy volunteers. *Neuropharmacology*
640 88:155–163 Available at:
641 <https://www.sciencedirect.com/science/article/pii/S0028390814003001> [Accessed January 3,
642 2019].

643 Pascual-Marqui RD, Michel CM, Lehmann D (1994) Low resolution electromagnetic tomography: a
644 new method for localizing electrical activity in the brain. *Int J Psychophysiol* 18:49–65 Available
645 at: <http://linkinghub.elsevier.com/retrieve/pii/016787608490014X> [Accessed December 18,
646 2018].

647 Phillips HN, Blenkman A, Hughes LE, Bekinschtein TA, Rowe JB (2015) Hierarchical Organization of
648 Frontotemporal Networks for the Prediction of Stimuli across Multiple Dimensions. *J Neurosci*
649 35:9255–9264 Available at: <http://www.ncbi.nlm.nih.gov/pubmed/26109651> [Accessed May 1,
650 2018].

651 Phillips HN, Blenkman A, Hughes LE, Kochen S, Bekinschtein TA, Cam-CAN, Rowe JB (2016)
652 Convergent evidence for hierarchical prediction networks from human electrocortigraphy
653 and magnetoencephalography. *Cortex* 82:192–205 Available at:
654 <https://www.sciencedirect.com/science/article/pii/S0010945216301058#fig3> [Accessed
655 January 15, 2019].

656 Port RG, Gaetz W, Bloy L, Wang D-J, Blaskey L, Kushner ES, Levy SE, Brodtkin ES, Roberts TPL (2017)
657 Exploring the relationship between cortical GABA concentrations, auditory gamma-band
658 responses and development in ASD: Evidence for an altered maturational trajectory in ASD.

659 Autism Res 10:593–607 Available at: <http://www.ncbi.nlm.nih.gov/pubmed/27696740>
660 [Accessed February 26, 2019].

661 Razi A, Kahan J, Rees G, Friston KJ (2015) Construct validation of a DCM for resting state fMRI.
662 Neuroimage 106:1–14 Available at:
663 <https://www.sciencedirect.com/science/article/pii/S1053811914009446> [Accessed September
664 13, 2018].

665 Roopun AK, Kramer MA, Carracedo LM, Kaiser M, Davies CH, Traub RD, Kopell NJ, Whittington MA
666 (2008a) Period concatenation underlies interactions between gamma and beta rhythms in
667 neocortex. Front Cell Neurosci 2:1 Available at:
668 <http://journal.frontiersin.org/article/10.3389/neuro.03.001.2008/abstract> [Accessed January 3,
669 2019].

670 Roopun AK, Kramer MA, Carracedo LM, Kaiser M, Davies CH, Traub RD, Kopell NJ, Whittington MA
671 (2008b) Temporal interactions between cortical rhythms. Front Neurosci 2:145–154 Available
672 at: <http://journal.frontiersin.org/article/10.3389/neuro.01.034.2008/abstract> [Accessed
673 January 3, 2019].

674 Roopun AK, LeBeau FEN, Rammell J, Cunningham MO, Traub RD, Whittington MA (2010) Cholinergic
675 neuromodulation controls directed temporal communication in neocortex in vitro. Front
676 Neural Circuits 4:8 Available at:
677 <http://journal.frontiersin.org/article/10.3389/fncir.2010.00008/abstract> [Accessed June 19,
678 2018].

679 Roopun AK, Middleton SJ, Cunningham MO, LeBeau FEN, Bibbig A, Whittington MA, Traub RD (2006)
680 A beta2-frequency (20-30 Hz) oscillation in nonsynaptic networks of somatosensory cortex.
681 Proc Natl Acad Sci U S A 103:15646–15650 Available at:
682 <http://www.ncbi.nlm.nih.gov/pubmed/17030821> [Accessed February 26, 2019].

683 Rowe JB, Hughes LE, Barker RA, Owen AM (2010) Dynamic causal modelling of effective connectivity

684 from fMRI: Are results reproducible and sensitive to Parkinson's disease and its treatment?
685 Neuroimage 52:1015–1026 Available at:
686 <https://www.sciencedirect.com/science/article/pii/S105381190901369X> [Accessed March 1,
687 2019].

688 Semyanov A, Walker MC, Kullmann DM, Silver RA (2004) Tonicly active GABAA receptors:
689 modulating gain and maintaining the tone. Trends Neurosci 27:262–269 Available at:
690 <https://www.sciencedirect.com/science/article/pii/S0166223604000906?via%3Dihub>
691 [Accessed June 18, 2018].

692 Shaw AD, Hughes LE, Moran RJ, Coyle-Gilchrist I, Rittman T, Rowe JB (2018) In vivo assay of cortical
693 microcircuitry in frontotemporal dementia: a platform for experimental medicine studies.
694 bioRxiv:416388 Available at: <https://www.biorxiv.org/content/early/2018/09/13/416388.short>
695 [Accessed November 7, 2018].

696 Shaw AD, Moran RJ, Muthukumaraswamy SD, Brealy J, Linden DE, Friston KJ, Singh KD (2017)
697 Neurophysiologically-informed markers of individual variability and pharmacological
698 manipulation of human cortical gamma. Neuroimage 161:19–31 Available at:
699 <http://www.ncbi.nlm.nih.gov/pubmed/28807873> [Accessed January 14, 2019].

700 Shipp S (2016) Neural Elements for Predictive Coding. Front Psychol 7:1792 Available at:
701 <http://journal.frontiersin.org/article/10.3389/fpsyg.2016.01792/full> [Accessed January 14,
702 2019].

703 Spriggs MJ, Sumner RL, McMillan RL, Moran RJ, Kirk IJ, Muthukumaraswamy SD (2018) Indexing
704 sensory plasticity: Evidence for distinct Predictive Coding and Hebbian learning mechanisms in
705 the cerebral cortex. Neuroimage 176:290–300 Available at:
706 <https://www.sciencedirect.com/science/article/pii/S105381191830380X> [Accessed January 15,
707 2019].

708 Stephan KE, Iglesias S, Heinzle J, Diaconescu AO (2015) Translational Perspectives for Computational

709 Neuroimaging. *Neuron* 87:716–732 Available at:
710 <https://www.sciencedirect.com/science/article/pii/S0896627315006303> [Accessed February
711 26, 2019].

712 Stephan KE, Kasper L, Harrison LM, Daunizeau J, den Ouden HEM, Breakspear M, Friston KJ (2008)
713 Nonlinear dynamic causal models for fMRI. *Neuroimage* 42:649–662 Available at:
714 <https://www.sciencedirect.com/science/article/pii/S1053811908005983> [Accessed February
715 26, 2019].

716 Sukov W, Barth DS (2001) Cellular mechanisms of thalamically evoked gamma oscillations in auditory
717 cortex. *J Neurophysiol* 85:1235–1245 Available at:
718 <http://www.physiology.org/doi/10.1152/jn.2001.85.3.1235> [Accessed June 18, 2018].

719 Symmonds M, Moran CH, Leite MI, Buckley C, Irani SR, Stephan KE, Friston KJ, Moran RJ (2018) Ion
720 channels in EEG: isolating channel dysfunction in NMDA receptor antibody encephalitis. *Brain*
721 141:1691–1702 Available at: <https://academic.oup.com/brain/article/141/6/1691/4990439>
722 [Accessed July 8, 2019].

723 Whittington M., Traub R., Kopell N, Ermentrout B, Buhl E. (2000) Inhibition-based rhythms:
724 experimental and mathematical observations on network dynamics. *Int J Psychophysiol*
725 38:315–336.

726 Whittington MA, Cunningham MO, LeBeau FEN, Racca C, Traub RD (2011) Multiple origins of the
727 cortical gamma rhythm. *Dev Neurobiol* 71:92–106 Available at:
728 <http://doi.wiley.com/10.1002/dneu.20814> [Accessed September 4, 2018].

729 Wu X, Huang L, Wu Z, Zhang C, Jiang D, Bai Y, Wang Y, Chen G (2013) Homeostatic competition
730 between phasic and tonic inhibition. *J Biol Chem* 288:25053–25065 Available at:
731 <http://www.ncbi.nlm.nih.gov/pubmed/23839941> [Accessed June 27, 2018].

732 Wyss C, Tse DHY, Komater M, Dammers J, Achermann R, Shah NJ, Kawohl W, Neuner I (2017) GABA

733 metabolism and its role in gamma-band oscillatory activity during auditory processing: An MRS
734 and EEG study. *Hum Brain Mapp* 38:3975–3987 Available at:
735 <http://www.ncbi.nlm.nih.gov/pubmed/28480987> [Accessed February 26, 2019].

736 Zeidman P, Jafarian A, Seghier ML, Litvak V, Cagnan H, Price CJ, Friston KJ (2019) A guide to group
737 effective connectivity analysis, part 2: Second level analysis with PEB. *Neuroimage* 200:12–25
738 Available at: <https://www.sciencedirect.com/science/article/pii/S1053811919305233>
739 [Accessed October 9, 2019].

740

741

742 **Figure Legends**

743 *Figure 1. The neuronal model.*

744 a. Intrinsic connectivities found in all nodes between layer 4 stellates (ss), inhibitory interneurons (ii),
745 superficial pyramidal modules (sp) and deep pyramidal modules (dp).

746 b. All 6 nodes used are represented as a network on the left, showing the extrinsic connectivities
747 (solid line = forward; dotted line = backward; dashed line = lateral). A left hemisphere representation
748 of these bilateral nodes in primary auditory cortex, superior temporal gyrus and inferior-frontal
749 gyrus (light, medium and dark grey, respectively).

750 c. A detailed view of the extrinsic population connections for forward (solid lines) and backward
751 (dotted lines) connections.

752 d. Matrices of the extrinsic and intrinsic connectivity weights, all of which had a permitted variance
753 of 1/16.

754 e. A process flow describing the steps taken in the meta-analysis phase.

755

756 *Figure 2. Event Related Fields (ERFs).*

757 a. Mean ERFs across all subjects for all six nodes for the standard and deviant trials from 0-380ms.

758 The difference wave (MMN) is also shown. ERFs from the placebo condition are shown in blue and
759 from the tiagabine condition in red. Significant changes with time across the drug condition are
760 shown as a thick black line within each axis ($p < 0.05$, Bonferroni corrected for 6 regions). Shaded
761 areas represent the standard error (SEM).

762 b. Significant differences for induced spectra power were found in the alpha (α), beta (β) and lower
763 and higher gamma bands (γ_1 and γ_2) (FWE cluster corrected at $p < 0.001$). Here they are shown as flat
764 scalp maps (lower plots) with rostro-caudal activity *versus* time (upper plots). The time axis runs
765 from 0–380 ms post-stimulus.

766 c. Source-reconstructed T-contrasts ($p < 0.001$) created for those frequency bands showing spatial
767 changes across the drug condition in the 135 – 235 ms time window.

768

769 *Figure 3. Comparison between model and data.*

770 a. Residual differences between the observed and model-generated ERFs are shown for both the
771 standard 4-cell conductance-based DCM and the ext-DCM. ERFs from all nodes for every subject are
772 concatenated along the y-axis.

773 b. Bayesian model comparison of the 4-cell conductance-based DCM and the ext-DCM favours the
774 ext-DCM, plotted here in terms of the posterior model probability (RFX Bayes Factor = 40.6).

775 c. Predicted ERFs are shown for the standard and deviant conditions, along with the difference wave
776 (Std–Dev). The placebo and tiagabine conditions are depicted in blue and red respectively with
777 significant differences ($p < 0.05$, Bonferroni corrected for 6 regions) shown as a thick black line within
778 each axis.

779 d. Correlation coefficient between prediction and data for each node and each condition. Boxplots
780 represent the distribution over subjects with small dots representing outliers and larger black circles
781 representing the correlation coefficient of the meaned response of all subjects for each node and
782 each condition.

783

784 *Figure 4. Prediction of hidden states.*

785 a. Significant differences in the modulation of GABA-A synaptic scaling for each of the three
786 symmetric nodes. Green/red show significantly greater/lesser GABA-A synaptic scaling for tiagabine
787 than the placebo. Posterior probability p-values are shown next to each connection.

788 b. To explore the functional differentiation between regions during the task conditions with respect
789 to tonic inhibition, tonic GABA-A scaling on deep interneurons in IFG, STG and Aud, for each

790 individual is plotted for the placebo and tiagabine conditions. The standard and deviant conditions
791 are plotted separately in the left and right columns respectively. Pair-wise Bayesian t-test statistics
792 are reported on each plot, showing the Bayes Factor for each of the 6 comparisons. When there is
793 evidence for a difference, or evidence for no difference, the Bayes factor is shown in green or blue
794 respectively.

795 c. The correlation demonstrates the dynamic balance that persists between phasic and tonic
796 inhibition (see main text discussion). Linear fit with 95% confidence bounds for tonic GABA-A scaling
797 on deep inhibitory neurons vs phasic GABA-A scaling from deep inhibitory neurons to thalamic
798 projecting pyramidals (Bayesian correlation pairs, Bayes factor=398.43).

799

800

801 *Table 1. Model parameters.*

802 Parameter values used by the neuronal model are shown with their permitted variances.

803

Parameter grouping	Parameter	Initial value	Permitted variance
Decay Constants, τ (ms)	AMPA τ	4	1/16
	NMDA τ	100	1/16
	GABAA τ	16	1/8
	GABAB τ	200	1/8
	$I_M \tau$	160	0
	$I_H \tau$	100	0
Misc. strengths	K ⁺ leak G	1	0
	Background V	2.17	1/32
Reversal potentials (mV)	Na ²⁺ reversal	60	0
	Ca ²⁺ reversal	10	0
	Cl ⁻ reversal	-90	0
	K ⁺ reversal	-70	0
	I_H reversal	-100	0
Firing threshold (mV)	V_T (all pops)	-40	0
Firing precision	V_X (all pops)	1	1/32
I_H I-V slope	V_{HX}	300	0
Cell Capacitances (pF)	ss_C	200	1/32
	sp_C	150	1/32
	si_C	50	1/32
	dp_C	400	1/32
	di_C	50	1/32
	tp_C	200	1/32
Delays (ms)	intrinsic	2	1/32
	extrinsic cortico-cortical	16	1/32
	extrinsic thalamo- cortical	80	1/32

Table 1

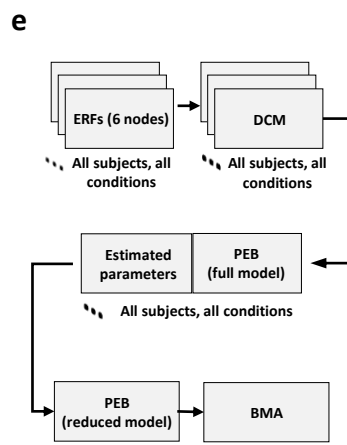
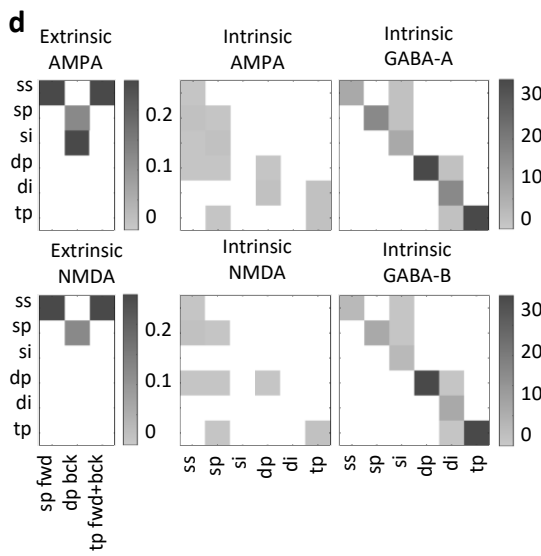
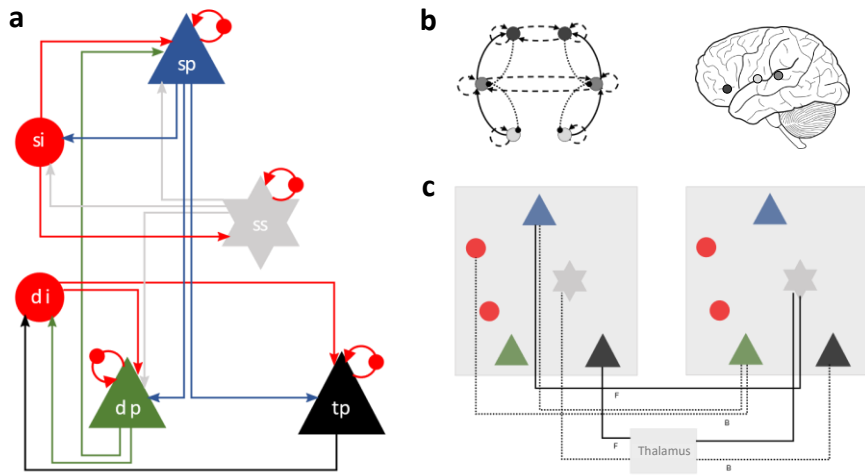
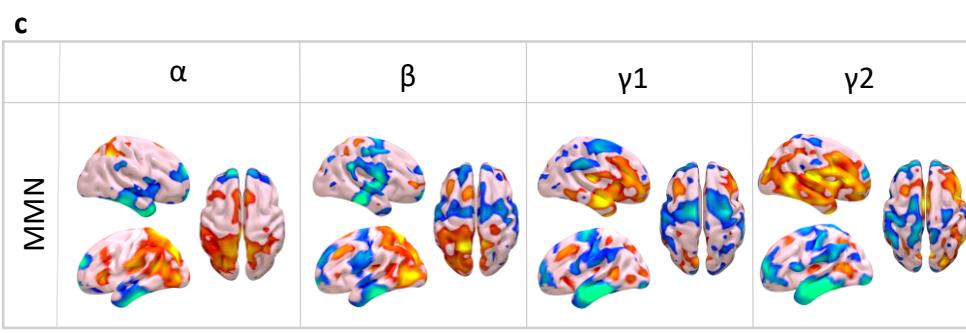
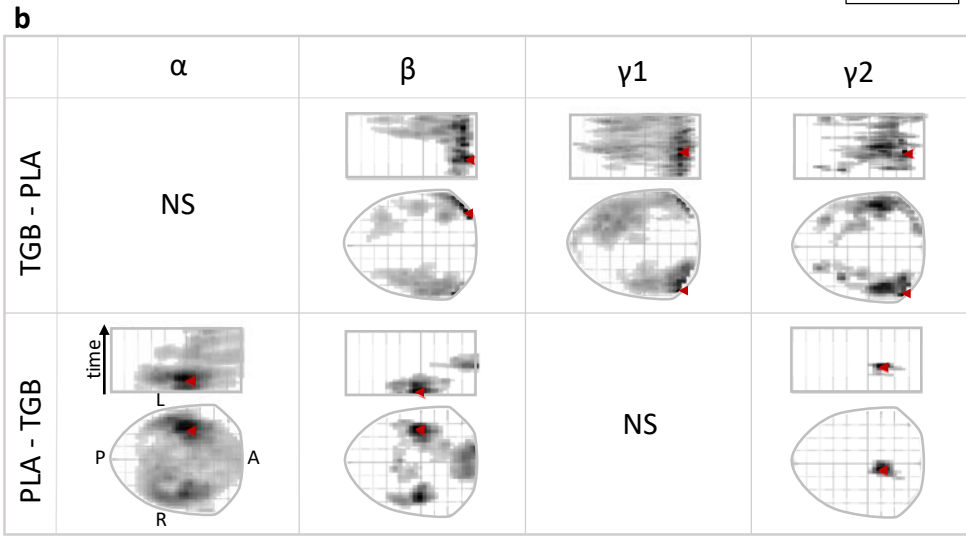
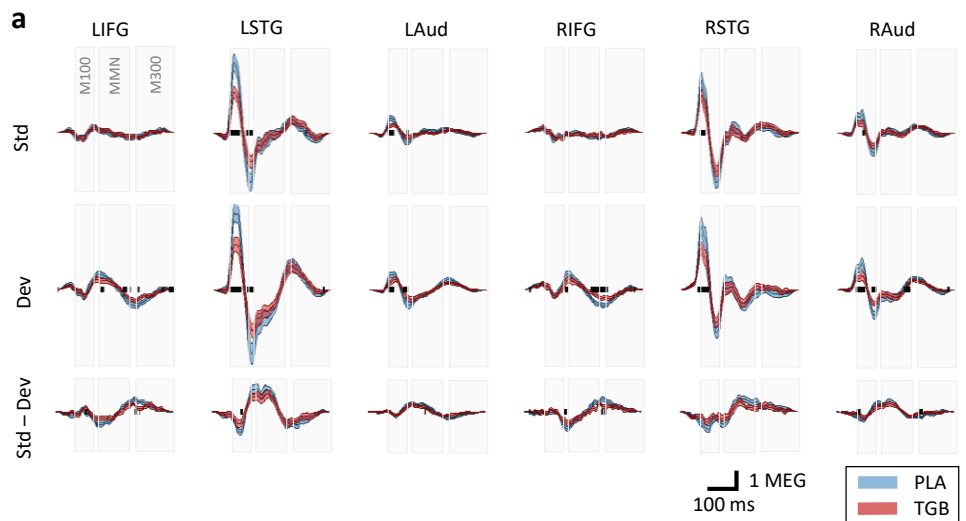


Figure 1



Tiagabine > Placebo (i.e. the top row in 'b')
 Tiagabine < Placebo (i.e. the bottom row in 'b')
 3.31 15

Figure 2

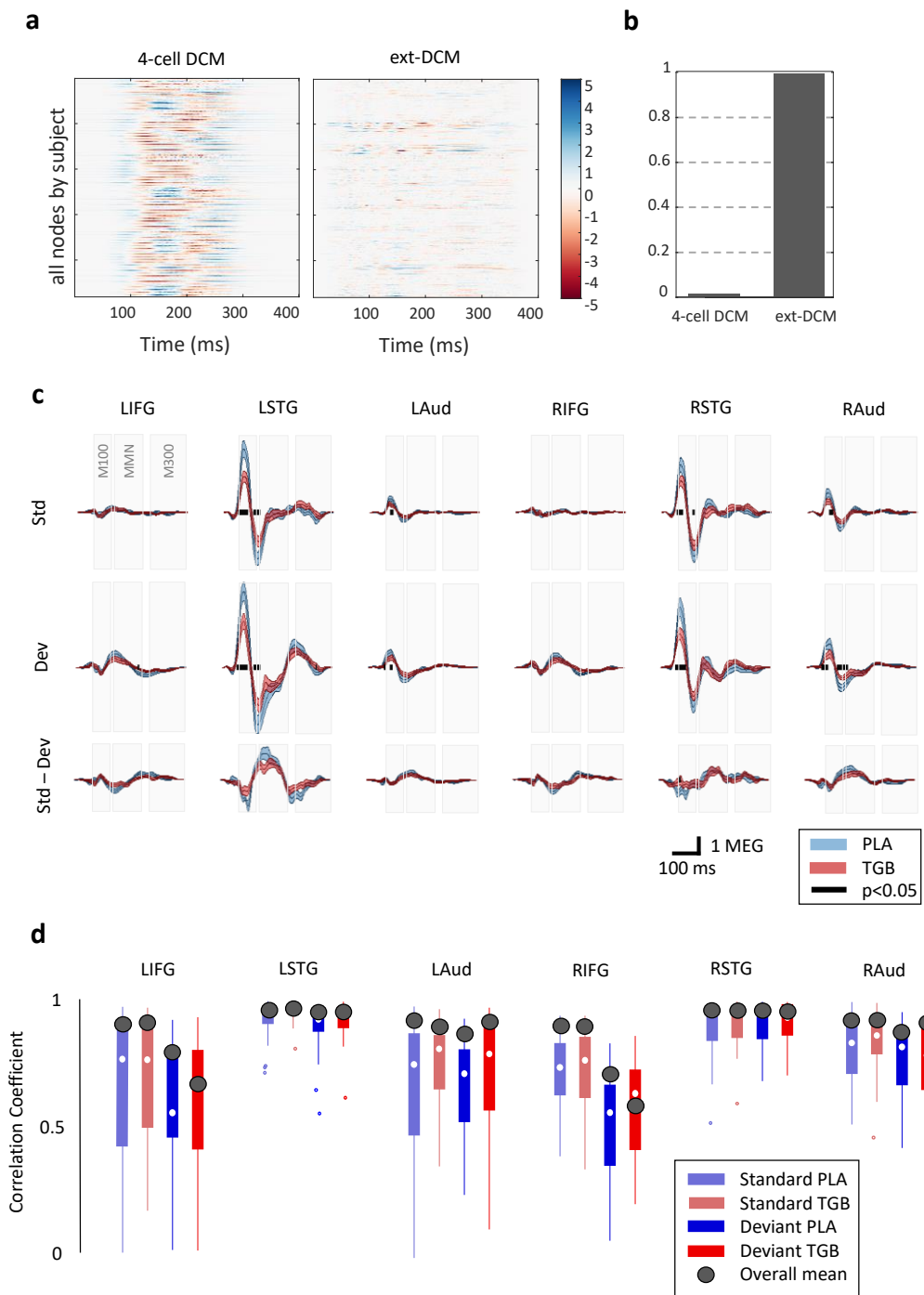


Figure 3

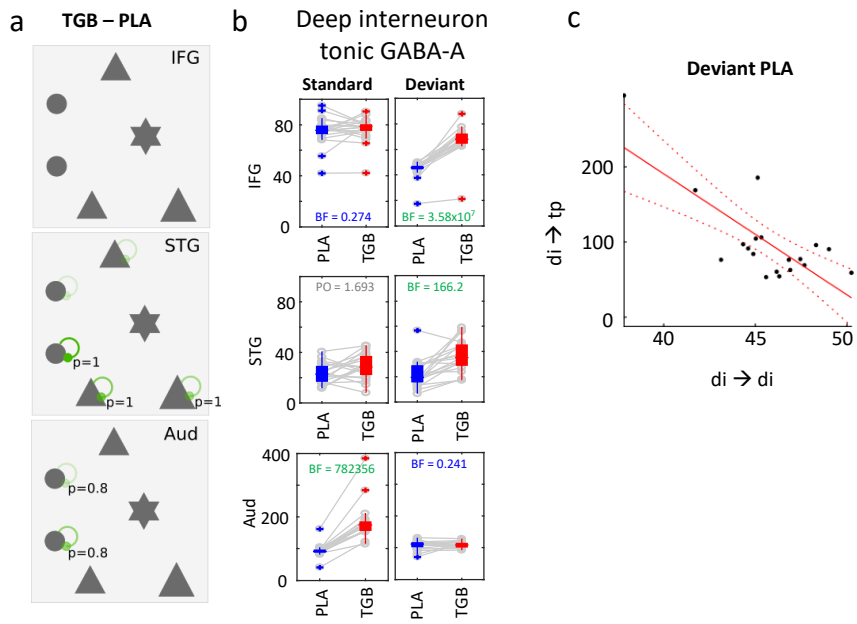


Figure 4